Journal of Materials Chemistry A

ROYAL SOCIETY OF CHEMISTRY

PAPER

View Article Online
View Journal

Cite this: DOI: 10.1039/d4ta02102a

Nitridation-boosted V e_g occupation of a VN@CNT flexible electrode for high-rate Zn-ion hybrid supercapacitors†

Yuyang Cao, Shiqiang Wei,* Yujian Xia, Quan Zhou, Yixiu Wang, Wenjie Xu, Changda Wang, Shuangming Chen* and Li Song

Flexible zinc-ion hybrid supercapacitors (f-ZHSCs), with their inherent safety, combine the advantages of the high power density of supercapacitors and the high energy density of zinc-ion batteries, making them a promising energy supply device for wearable and implantable devices. However, commonly used rigid cathode materials and fracture-prone metallic current collectors encounter significant challenges, such as inadequate flexibility and compromised cycling stability, which impede the further development of f-ZHSCs. Herein, we design a free-standing flexible membrane electrode VN@CNT for f-ZHSCs through a nitridation strategy. Soft X-ray absorption spectroscopy (s-XAS) reveals the boosted occupation of electrons in the V e_g orbital $3d_{x^2-y^2}$ state after nitridation, leading to enhanced metallicity and conductivity. As a result, the VN@CNT flexible electrode exhibits an excellent specific capacitance of 314.44 F g^{-1} at 0.5 A g^{-1}. Moreover, it demonstrates exceptional rate capability, retaining 80.17% of its capacitance at a high current density of 10 A g^{-1} compared to that of 0.5 A g^{-1}. Importantly, it also shows excellent flexibility, enduring bending angles of 0 to 180° and showing no detectable degradation in capacitance after 1200 bending cycles. By design and in-depth study of the local structure of the flexible electrode, this work provides insight into the development of flexible electronics.

Received 29th March 2024
Accepted 13th June 2024

DOI: 10.1039/d4ta02102a

rsc.li/materials-a

1 Introduction

The rapid advancement of flexible electronic devices in recent years has been driven by the growing demand for wearable and portable technology, which not only has the potential to revolutionize next-generation electronic devices but also significantly impact and shape people's daily lives.[1–4] However, the development of flexible electronics is heavily reliant on the availability of safe and high-performance flexible energy storage solutions.[5] While flexible lithium-ion batteries have made substantial strides,[6,7] the inherent flammability of commonly used organic electrolytes (such as EC and DEC) raises safety concerns, making them unsuitable for meeting the rigorous safety standards required for wearable and implantable applications.[8,9] Among the various energy storage technologies, aqueous ZHSCs have surfaced as promising candidates for developing flexible energy storage devices due to their intrinsic high safety and high power density.[10–15] However, achieving high-performance f-ZHSCs still presents significant challenges.[16] Firstly, commonly used electrode active materials (such as activated carbon[17] and metal oxides[18]) are predominantly rigid and possess poor mechanical flexibility, making them prone to fracture, delamination, and other failure mechanisms under repeated bending strains. Secondly, metallic current collectors (such as stainless steel), despite their outstanding electrical conductivity, have limited flexibility and poor fatigue resistance, making them susceptible to fracture under dynamic stress, which severely limits the cycling stability of the devices.

To tackle these challenges, *in situ* growth has been regarded as an effective electrode preparation strategy. Wang *et al.*[19] reported a cable-like V_2O_5 structure *in situ* grown on carbon cloth for constructing flexible zinc-ion batteries, simultaneously addressing the flexibility issues of both the electrode material and current collector. However, this method typically requires the use of relatively thick carbon cloth as the substrate, significantly reducing the energy density of the electrodes and hindering their further commercialization. Recently, various novel flexible conductive substrates, such as carbon paper[20] and graphene films,[21] have emerged, exhibiting outstanding mechanical flexibility. Nevertheless, the insufficient intrinsic conductivity of these substrate materials limits the full utilization of the electrochemical performance of the active electrode materials, leaving a gap between current performance and practical application requirements.

National Synchrotron Radiation Laboratory, CAS Center for Excellence in Nanoscience, University of Science and Technology of China, Hefei 230029, P. R. China. E-mail: sqw@ustc.edu.cn; csmp@ustc.edu.cn

† Electronic supplementary information (ESI) available. See DOI: https://doi.org/10.1039/d4ta02102a

In this work, we develop a free-standing flexible membrane electrode, VN@CNT, as a cathode material for ZHSCs, and its local structure, electrochemical performance, and flexibility were comprehensively studied. s-XAS revealed increased electron occupation in the V e_g orbital $3d_{x^2-y^2}$ state after nitridation from V_2C@CNT to VN@CNT, leading to a reduction in the valence state of V. This significantly enhanced the metallicity and electrical conductivity of VN@CNT, with the van der Pauw method showing a nearly tenfold increase in conductivity to 2.48×10^4 S m^{-1} after nitridation. Consequently, the VN@CNT electrode exhibited a high specific capacitance of 252.09 F g^{-1} even at a high discharge rate of 120 C, retaining 80.17% of its capacitance compared to that at 1.6 C. Notably, the f-ZHSC assembled with VN@CNT demonstrated exceptional flexibility, maintaining stable discharge curves and capacitance at various bending angles ranging from 0° to 180°. Remarkably, the device demonstrated an enhancement in capacitance after being subjected to 1200 bending cycles, surpassing its initial performance, showcasing its outstanding mechanical flexibility and long-term usability. This study highlights the importance of innovative material design and thorough investigation of the local structure of materials in achieving excellent electrochemical performance as well as flexibility, thus paving the way for the development of advanced flexible electronic devices.

2 Experimental section

2.1 Synthesis of V_2C MXene

V_2AlC MAX with a particle size of 400 mesh was purchased from Jilin 11 Technology Co., Ltd. V_2C was obtained by etching V_2AlC with a mixture of HCl and LiF. Typically, 30 mL of HCl (98%) and 2 g of LiF were mixed uniformly. This mixture was then slowly added to the inner liner of a 50 mL reaction vessel containing 0.5 g of V_2AlC MAX. The vessel was placed on a rotary heating plate inside a fume hood and the mixture was stirred at a constant temperature of 70 °C for 7 days. After the reaction, the mixture was allowed to settle and cool to room temperature (care must be taken when handling fluoride-containing acidic solutions to ensure safety). The supernatant was removed and 30 mL of hydrochloric acid was added to remove any residual LiF. After the reaction, the supernatant was again removed, and the remaining liquid was subjected to centrifugation with water or anhydrous ethanol at a speed of 8000 rpm per minute. This process was repeated five times or until the pH of the supernatant reached 7. The powder obtained by centrifugation was then placed in a freeze dryer with a −60 °C cold trap for 12 hours until fully dried, yielding V_2C MXene.

2.2 Synthesis of d-V_2C

Delaminated V_2C (denoted as d-V_2C) samples were obtained following the synthesis process reported in our previous work.[22] Briefly, 6 mL of 25% TMAOH and 0.5 g of V_2C MXene were mixed evenly and stirred at 500 rpm for 8 hours. The reaction product was then centrifuged at 8000 rpm for 5 minutes, which was repeated twice to remove excess TMAOH. Subsequently, the product was placed in an ultrasonic disruptor and sonicated for 30 minutes at a low temperature of 5 °C. Then, the resulting solution was centrifuged at a speed of 3000 rpm for 10 minutes. The supernatant was collected and frozen under liquid nitrogen before being placed into a freeze-dryer for 4 days to obtain d-V_2C.

2.3 Synthesis of V_2C@CNT, A-V_2C@CNT, and VN@CNT flexible membranes

V_2C@CNT and VN@CNT flexible membranes were assembled *via* a vacuum filtration process. Typically, 1 mg of single-walled carbon nanotubes (SWCNT), 9 mg of d-V_2C, and 20 mg of CTAB (cetyltrimethylammonium bromide) were placed in an ultrasonic disruptor and sonicated for 40 minutes at a low temperature of 5 °C. The mixture was then transferred to a vacuum filtration apparatus to form the membrane. The membrane was then washed with a total of 100 mL of deionized water in small increments to remove residual CTAB. After that, the membrane was washed with acetone to remove the water-based mixed fiber membrane used as a support, yielding the V_2C@CNT membrane. Finally, the obtained sample was placed in a tube furnace and annealed under a 99.9% ammonia atmosphere at 600 °C for 2 hours, and then naturally cooled to room temperature to obtain the VN@CNT membrane. Under the same annealing temperature and duration as VN@CNT, annealing in an argon atmosphere produces annealed V_2C@CNT (denoted as A-V_2C@CNT).

2.4 Assembly and fabrication of coin-type ZHSCs and pouch-type f-ZHSCs

To assemble the coin-type ZHSCs, the as-abstained VN@CNT flexible membrane was cut into circular discs with a diameter of 12 mm to function as the cathode. GF/C, with a diameter of 20 mm, was utilized as a separator. Zinc metal foil, also with a diameter of 12 mm, was employed as the anode. These components were layered and incorporated into a coin-cell casing along with 100 μL of a 3 M $Zn(CF_3SO_3)_2$ solution, serving as the electrolyte. The aforementioned components were assembled into a CR2032 button cell in the air.

For the construction of the pouch-type f-ZHSCs, layers consisting of the VN@CNT membrane, GF/C separator, and zinc foil were assembled in descending order and encapsulated within a 9 cm × 8 cm pouch made of an aluminum–plastic laminate. Nickel tabs, measuring 0.1 mm in thickness, 2 mm in width, and 60 mm in length, and coated with a sealing adhesive, were affixed to both the VN@CNT composite and the zinc foil to create external electrical leads. Before the final sealing step, 600 μL of a 3 M $Zn(CF_3SO_3)_2$ solution was introduced into the pouch as the electrolyte. The packaging process was completed with the aid of a vacuum sealing machine, which first evacuated the pouch for 30 seconds and then heat-sealed it at 130 °C for another 30 seconds to create a vacuum environment, thereby finalizing the creation of the f-ZHSC.

2.5 Electrochemical characterization

All electrochemical tests were conducted on a CHI760E, a CHI660E electrochemical workstation, and a LAND CT2001A

battery tester. The mass of the active material was determined from the total weight of the membrane after nitridation. For galvanostatic charge/discharge (GCD) testing methods, the specific capacitance of the device was calculated according to the following eqn (1):

$$C_m = \frac{I\Delta t}{m\Delta V} \quad (1)$$

For CV testing methods, the specific capacitance of the device was calculated according to eqn (2):

$$C_{\mathrm{m}} = \frac{\int I\mathrm{d}V}{\Delta V m\, v} \quad (2)$$

In the aforementioned formula, C_{m} represents specific capacitance with the unit of F g^{-1}, I is the current, m is the mass of the membrane, Δt is the discharge time, and ΔV is the voltage without IR drop. $\int I\mathrm{d}V$ is the integral of the current (I) with respect to voltage (V) over one complete cycle of the cyclic voltammetry scan, representing the total charge transferred between the voltage limits. v denotes the scan rate of the voltage.

2.6 Material characterization

X-ray diffraction (XRD) patterns were recorded on a sample horizontal high-power X-ray diffractometer (Rigaku TTRIII, Cu Kα, $\lambda = 1.54178$ Å). Scanning Electron Microscopy (SEM) characterization was performed using a Field Emission Scanning Electron Microscope (SEM at 2 kV, Zeiss Gemini360). Transmission Electron Microscopy (TEM) images, High-Resolution TEM (HRTEM) images, and Energy-Dispersive X-ray Spectroscopy (EDS) images were captured using a JEOL JEM-2100 Plus instrument operating at 200 kV. Transport measurements were performed using a PPMS setup (Quantum Design DynaCool system). The Vander Pauw method was used to measure electrical transport. V L-edge XANES measurements were carried out at the beamlines BL11U, BL10B, MCD-A, and MCD-B S at the National Synchrotron Radiation Laboratory (NSRL). XAFS measurements were performed in transmission mode at the beamline 1W1B of the Beijing Synchrotron Radiation Facility (BSRF). *In situ* XRD patterns were obtained at the beamline BL14B1 in the Shanghai Synchrotron Radiation Facility (SSRF). The WinXAS program was used to analyze XAFS data.[23]

3 Results and discussion

The VN@CNT flexible electrode was obtained *via* a vacuum filtration process, followed by a nitridation strategy. The detailed preparation process is described in the Experimental section. The X-ray diffraction (XRD) patterns of the achieved product, as shown in Fig. 1a, indicate the presence of only the (002) peak in V_2C@CNT, confirming the successful removal of the Al component after etching and delamination.[22,24,25] Moreover, the forward shift of the (002) peak after delamination suggests an increase in the interlayer distance,[22] and the XRD before delamination is provided in Fig. S1 in the ESI.† Upon

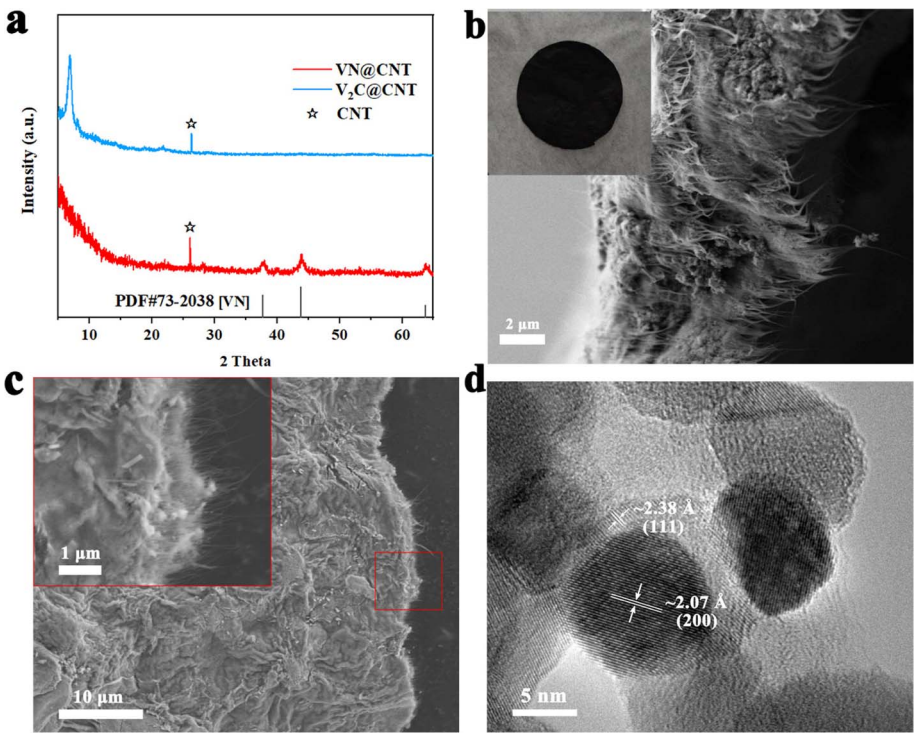

Fig. 1 Characterization of VN@CNT and V_2C@CNT. (a) XRD patterns of VN@CNT and V_2C@CNT, respectively. (b) SEM images of the cross-section of the VN@CNT flexible membrane, and the inset shows the VN@CNT membrane electrode (c). SEM images of the vertical view of the VN@CNT flexible membrane and the inset shows a partially enlarged image. (d) HRTEM image of VN@CNT.

nitridation, the characteristic (002) peak vanishes, and new diffraction peaks emerge corresponding to the (111) and (200) planes, characteristic of cubic VN.[26] This transformation is indicative of a phase transition from the layered delaminated V_2C to the cubic crystal structure of VN. It is noteworthy that the cross-sectional view from Fig. 1b reveals a tightly stacked VN@CNT membrane, with VN and CNT uniformly dispersed, forming a cross-stacked structure. This uniformity is also confirmed by the EDS mapping in Fig. S2,† particularly for V and N, which exhibit a highly uniform distribution throughout the entire membrane. Furthermore, the top view of the VN@CNT membrane in Fig. 1c and its corresponding high-magnification image displays a tight interconnection between VN and the carbon nanotube network. This unique architecture not only provides excellent flexibility but also establishes an effective conductive network, enhancing the accessibility of the VN layers to electrolytic ions, thereby promoting superior energy storage performance. As indicated by the TEM image in Fig. S3,† the anchoring of VN nanoparticles on CNTs remains robust even after ultrasonication to create a suspension. The VN particles exhibit an extremely small particle size, around 10 nm, which is significantly different from bulk commercial vanadium nitride (denoted as C-VN), as depicted in the SEM image shown in Fig. S4.† The HRTEM image of VN@CNT reveals two distinct lattice spacings of 0.207 nm and 0.238 nm (Fig. 1d), which correspond to the (111) and (200) planes of cubic VN,[27] respectively, confirming the results obtained from XRD analyses.

To investigate the electronic structure of VN@CNT, techniques such as s-XAS, X-ray photoelectron spectroscopy (XPS), and X-ray absorption fine structure (XAFS) were employed. As illustrated in Fig. 2a, the reduction of vanadium was evidenced from the perspective of electronic transition. Within the pre-edge region, the peak located at 517.8 eV in C-VN corresponds to the V $3d_{xy}$ state, which is the lowest unoccupied state in the V t_{2g} orbitals.[28,29] The peak positioned at 519.6 eV in V_2C@CNT exhibits the unoccupied characteristics of the $3d_{x^2-y^2}$ state in the V e_g orbitals.[29–31]. In VN@CNT, the peak at 517.8 eV disappears, indicating electron occupancy in the $3d_{xy}$ state. Similarly, the peak at 519.6 eV also disappears with an increase in the width and a decrease in resonance after nitridation, indicating electron occupation in the $3d_{x^2-y^2}$ state.[32] The occupation of electrons in both V t_{2g} and e_g orbitals suggests that VN undergoes a reduction to a lower valence state upon composite formation and nitridation,[28] which is beneficial to electron transfer.[33] Comparing V_2C@CNT with VN@CNT, the peaks at the L_2 and L_3-edges both shift towards lower energies after nitridation, confirming the reduction of V and the decrease in its valence state.[22,24,34] The significant reduction in the area under the L_2 and L_3-edge peaks also corroborates the increased metallic nature of VN@CNT.[35,36] These changes indicate an enhancement in metallic character, which usually leads to improved electrical conductivity. The conductivities of VN@CNT and V_2C@CNT were further determined by the Van-der Pauw method, as shown in Table S1 and Fig. S5,† where the

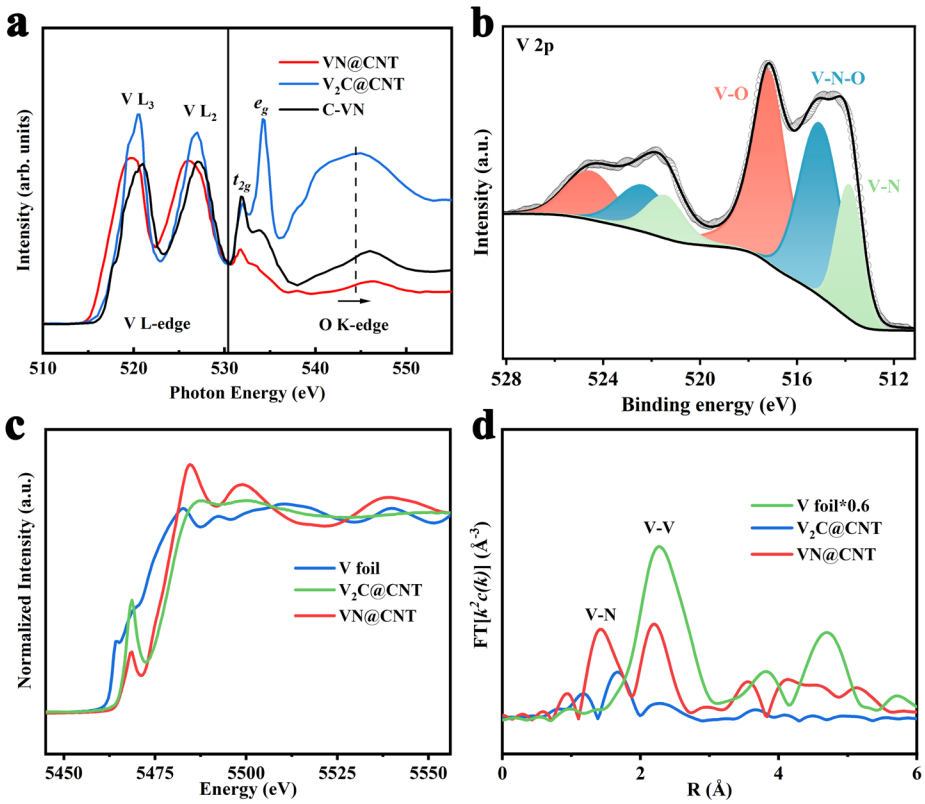

Fig. 2 X-ray spectroscopy characterization of the electronic structure of VN@CNT and V_2C@CNT. (a) V L-edge and O K-edge s-XAS spectra of VN@CNT, V_2C@CNT and c-VN. (b) High-resolution V 2p XPS spectra of VN@CNT. (c) Normalized XANES spectra of the V K-edge for VN@CNT, V_2C@CNT and V foil, and (d) Fourier-transformed V K-edge EXAFS spectra of VN@CNT, V_2C@CNT, and V foil × 0.6.

conductivity increased from 2.20 × 10^3 S m^{-1} to 2.48 × 10^4 S m^{-1} after nitridation. This over tenfold increase in conductivity significantly accelerates the electron transfer capability of VN@CNT, which is beneficial for accelerating the charge transfer rate inside the electrode, thereby improving the electrode's rate performance.[37–39] The I–V curve of the membrane is presented in Fig. S6,† revealing the ohmic contact behavior and outstanding electrical conductivity of the material. At the O K-edge, the attenuation of the t_{2g} and e_g intensities is related to the occupation of the 3d orbitals by electrons and the distortion of the structure.[40] After nitridation, the peak at 545.0 eV shifts to 546.0 eV, which is associated with the distortion of the V–O bond structure.[41]

The formation of V–N bonds and the overall reduction in the valence state were further characterized by XPS. For V_2C@CNT, a pair of peaks located at 516.10 and 523.25 eV correspond to V^{4+} (Fig. S7†),[28] while another pair at 517.35 and 524.55 eV corresponds to V^{5+}.[22] In the case of VN@CNT, two peaks at 513.85 and 521.5 eV correspond to V–N (Fig. 2b). The remaining two pairs of peaks located at 515.13 and 522.45 and at 517.2 and 524.6 eV are associated with V–N–O and V–O, respectively.[26] By deconvoluting the N 1s spectrum, three chemical states of nitrogen species can be identified in VN@CNT. The corresponding subpeaks shown in Fig. S8† are located at 397.25, 398.95, and 401.25 eV, which can be attributed to the metal–nitride bond (V–N), pyrrolic nitrogen, and graphitic nitrogen, respectively.[42] After nitridation, there is a substantial shift of the binding energies towards lower values, indicating that vanadium gains electrons and the overall valence state of vanadium is reduced after nitridation.[29] This observation is consistent with the results obtained from s-XAS.

The analysis of the V K-edge XANES spectra is shown in Fig. 2c. Due to the sensitivity of the pre-edge peak to the local coordination environment of the absorbing atom and the density of d-state electrons, it can be used to evaluate changes in the local symmetry of the V atoms.[43] Compared to V_2C@CNT, the V atoms in VN@CNT exhibit higher local symmetry due to the structural symmetry brought about by the cubic phase crystal structure of VN.[22] The edge energy of VN@CNT shifts to a lower position compared to V_2C@CNT, indicating that V is reduced and its valence state is lowered after nitridation, which is consistent with the previous characterization. The Fourier-transformed Extended X-ray Absorption Fine Structure (EXAFS) spectra in *R*-space of the V K-edge for V_2C@CNT, as shown in Fig. 2d, display a lower peak intensity corresponding to the V–V bond, suggesting that delaminated V_2C MXene is close to isolated monolayers after delamination with only in-plane V–V bonding. However, after nitridation, the intensity of the V–V bond significantly increases due to the transformation of monolayer V_2C into cubic phase VN, where the structure recombines and V–V bonds are established.

To investigate the electrochemical performance of the VN@CNT membrane electrode and its application in ZHSCs, we fabricated VN@CNT//Zn ZHSCs using zinc foil as the counter electrode and 3 M $Zn(CF_3SO_3)_2$ aqueous solution as the electrolyte.

As illustrated in Fig. 3a, the cyclic voltammetry (CV) curves of the Zn//VN@CNT supercapacitors were recorded at different

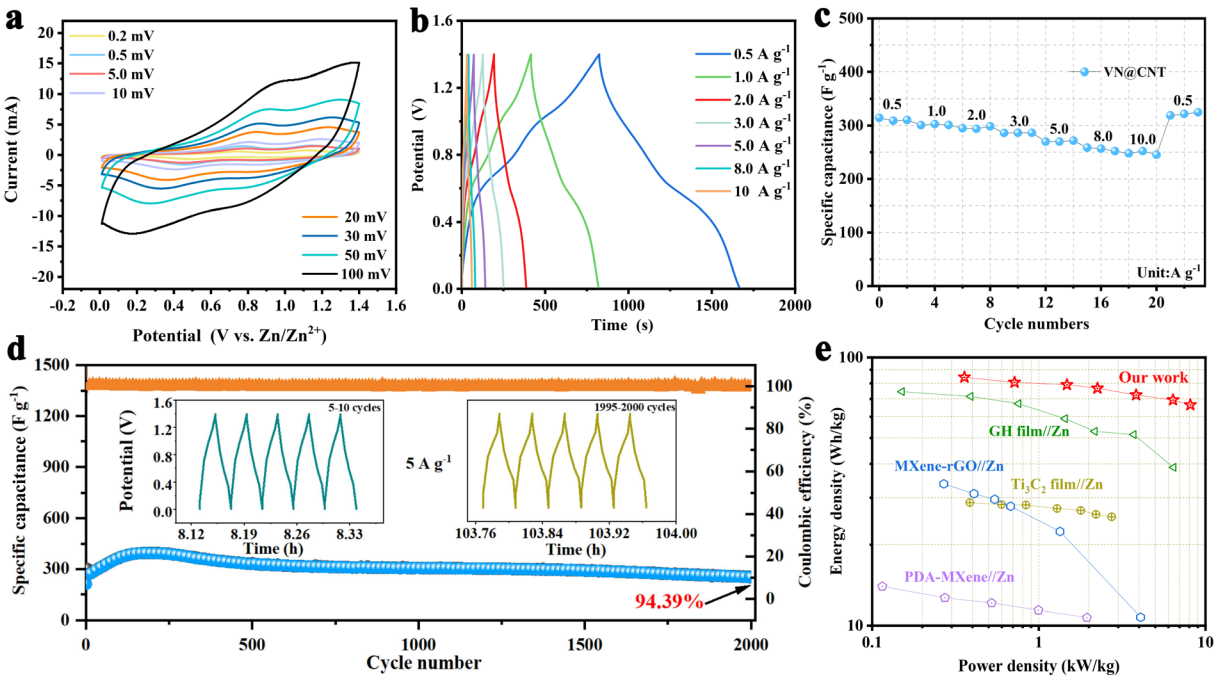

Fig. 3 Electrochemical performance of the VN@CNT cathode for ZHSCs. (a) CV curves at the scan rates of 0.2 to 100 mV s^{-1}. (b) GCD curves at the densities of 0.2 to 10 A g^{-1}. (c) Rate capability at different current densities. (d) Cycling stability of VN@CNT at 5 A g^{-1} and the inset shows the GCD curves of 5–10 cycles and 1995–2000 cycles. (e) The Ragone plots of ZHSCs assembled with the VN@CNT membrane electrode, comparing this work with other ZHSC studies.

scan rates ranging from 0.2 to 100 mV s^{-1}, within a voltage window from 0.01 V to 1.40 V. The CV curves exhibit a quasi-rectangular shape with distinct redox peaks, indicating that the CV response of the device encompasses both double-layer capacitance behavior and battery-like reactions.[44–46] As the scan rate increased up to 100 mV s^{-1}, the shape of the CV curves remained essentially unchanged, demonstrating excellent reaction kinetics and energy storage capability of the VN@CNT electrode during charge–discharge processes.[47] Additionally, the two pairs of redox peaks located at approximately 0.844/0.358 V and 1.215/0.861 V could correspond to the continuous desorption and adsorption of Zn^{2+} ions.[48] Within the same voltage window, the GCD curves of the VN@CNT//Zn ZHSC were recorded at different current densities ranging from 0.5 A g^{-1} to 10 A g^{-1} (Fig. 3b), exhibiting typical near-isosceles triangular shapes, indicative of high reversibility during the charge–discharge processes. The specific capacitance calculated from the GCD discharge curves at various current densities is illustrated in Fig. 3c. At a current density of 0.5 A g^{-1}, a specific capacitance of 314.44 F g^{-1} is exhibited. Due to the high conductivity, even when the current density is increased by 20 times to 10 A g^{-1} (120 C), a capacitance of 243.542 F g^{-1} is still maintained, retaining 80.17% of the capacitance compared to that at 0.5 A g^{-1}. Remarkably, when the current is restored from 10 A g^{-1} to 0.5 A g^{-1}, the capacitance can rebound to 318.89 F g^{-1}. To further evaluate the rate capability of the material, GCD tests were conducted over a wider range of current densities. Fig. S9† shows that even at 15 and 20 A g^{-1}, the material still maintains a considerable capacity retention rate, demonstrating its exceptional rate performance, which is associated with the rise of conductivity after nitridation,[37] catering to the rapid charge–discharge needs and varying power requirements encountered in the daily use of flexible devices. Furthermore, due to the high usage frequency of flexible wearable devices, cycling stability is also a crucial performance metric in flexible electronics.[49] The cycling performance of the ZHSC is demonstrated in Fig. 3d. During the initial cycles, the specific capacitance exhibited a certain degree of increase, which can be attributed to the activation process of the material.[50–52] It is noteworthy that even after 2000 cycles at a current density of 5 A g^{-1}, the ZHSC maintained 94.39% of its initial capacitance. Notably, as shown in the inset in Fig. 3d, there is only a slight change between the first and the last five GCD curves at a current density of 5 A g^{-1}, evidencing excellent cycling stability. To evaluate the stability of the material during the cycling process, we performed SEM and TEM characterization on the electrode after 500 cycles to observe the morphological evolution and microscopic surface behavior of VN@CNT. As shown in Fig. S10a,† it can be clearly observed that even after undergoing 500 charge–discharge cycles, the membrane maintains a tightly connected state without any signs of particle aggregation or cracks. Further TEM and HRTEM analyses in Fig. S10b and c† reveal that the VN nanoparticles remain firmly anchored on the CNTs. These results confirm the exceptional stability and structural integrity of the VN@CNT composite material during long-term cycling. Comparative evaluation through GCD and CV tests showed that the V_2C@CNT and C-VN based ZHSCs underperformed relative to the VN@CNT-based ones, a finding that underscores the significant performance enhancements associated with higher electrical conductivity, with detailed results presented in Fig. S12 and 13.† To investigate the influence of the high-temperature annealing step during the material synthesis process on its performance, A-V_2C@CNT was synthesized to demonstrate the positive impact of nitridation. Fig S14† clearly shows that A-V_2C@CNT, which underwent high-temperature annealing treatment in an argon atmosphere, exhibits significantly inferior electrochemical performance compared to VN@CNT, which was subjected to nitridation treatment. This further confirms the remarkable improvement in the electrochemical properties of the material brought about by the nitridation process. As represented in the Ragone plots in Fig. 3e, the power density and energy density calculated from the GCD curves of VN@CNT were compared with those reported for other cathode materials (Ti_3C_2 film//Zn,[44] MXene-rGO//Zn,[53] GH film//Zn,[54] and PDA-MXene//Zn[55]), demonstrating the superior zinc-ion storage performance of VN@CNT. At a power density of 357.80 W kg^{-1}, the device exhibits an energy density of 84.38 W h kg^{-1}, and when the power density is increased by nearly 22 times to 8118.06 W kg^{-1}, the device still retains 78.83% of the energy density at 66.52 W h kg^{-1}, which indicates that the device is capable of delivering high power output and long-term usage while also having advantages in terms of size and weight.

To further investigate the energy storage mechanism behind the exceptional electrochemical performance of VN@CNT, additional studies are presented in Fig. 4. Fig. 4a illustrates the adsorption–desorption process of Zn^{2+} on the surface of the VN@CNT membrane electrode during the charge–discharge cycles, while Fig. 4b displays the *in situ* XRD patterns of the VN@CNT membrane electrode during the charge–discharge cycles, characterized by synchrotron radiation based *in situ* XRD. Throughout the entire charge–discharge process, the positions of the diffraction peaks corresponding to the (111) and (200) planes of VN remained unchanged, indicating that Zn^{2+} did not intercalate into the VN crystal lattice during the discharge process, suggesting that the energy storage mechanism for Zn^{2+} is based on surface adsorption–desorption. After one complete charge–discharge cycle, the characteristic peaks stayed at their original positions, and no change in the crystal structure was observed, indicating that the VN@CNT electrode possesses good cycling performance as an electrode material.[56]

As the interest and research in flexible wearable electronics continue to grow, flexible devices that combine electrochemical and bending performance have become an important research direction in the field of energy storage.[57,58] In line with this trend, we have fabricated an f-ZHSC device with soft Zn foil, a separator, a VN@CNT membrane electrode, and an electrolyte. The schematic diagram of the device assembly is shown in Fig. 5a, and the specific fabrication process is detailed in the Experimental section. Electrochemical performance tests based on flexibility have been further provided. For flexible and wearable electronic devices that frequently encounter bending in daily use, their electrochemical performance under various bending states is particularly critical. GCD tests were conducted on the f-ZHSC in

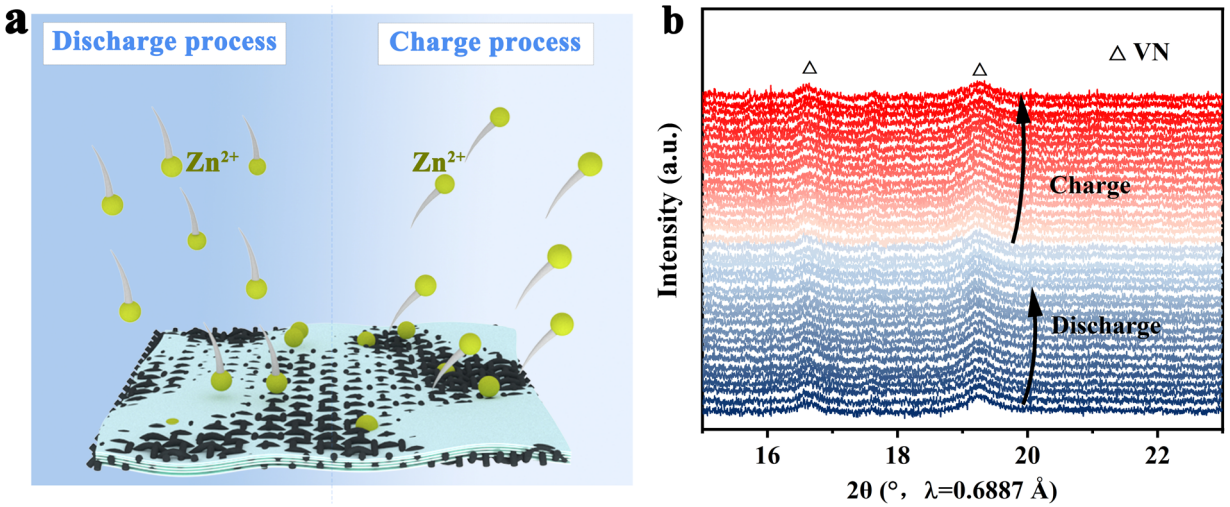

Fig. 4 (a) Schematic illustration of the discharge and charge process of the VN@CNT membrane electrode. (b) *In situ* synchrotron radiation XRD patterns of the VN@CNT membrane electrode during the first discharge/charge cycle.

a flat state and at bending angles of 30°, 60°, 90°, and 180° under a current density of 0.5 A g^{-1}, with the results shown in Fig. 5b. It can be observed that the discharge curves and capacitance values remain consistent whether the device is flat or bent at various angles. This demonstrates the excellent flexibility of the device and highlights the potential application of VN@CNT membrane

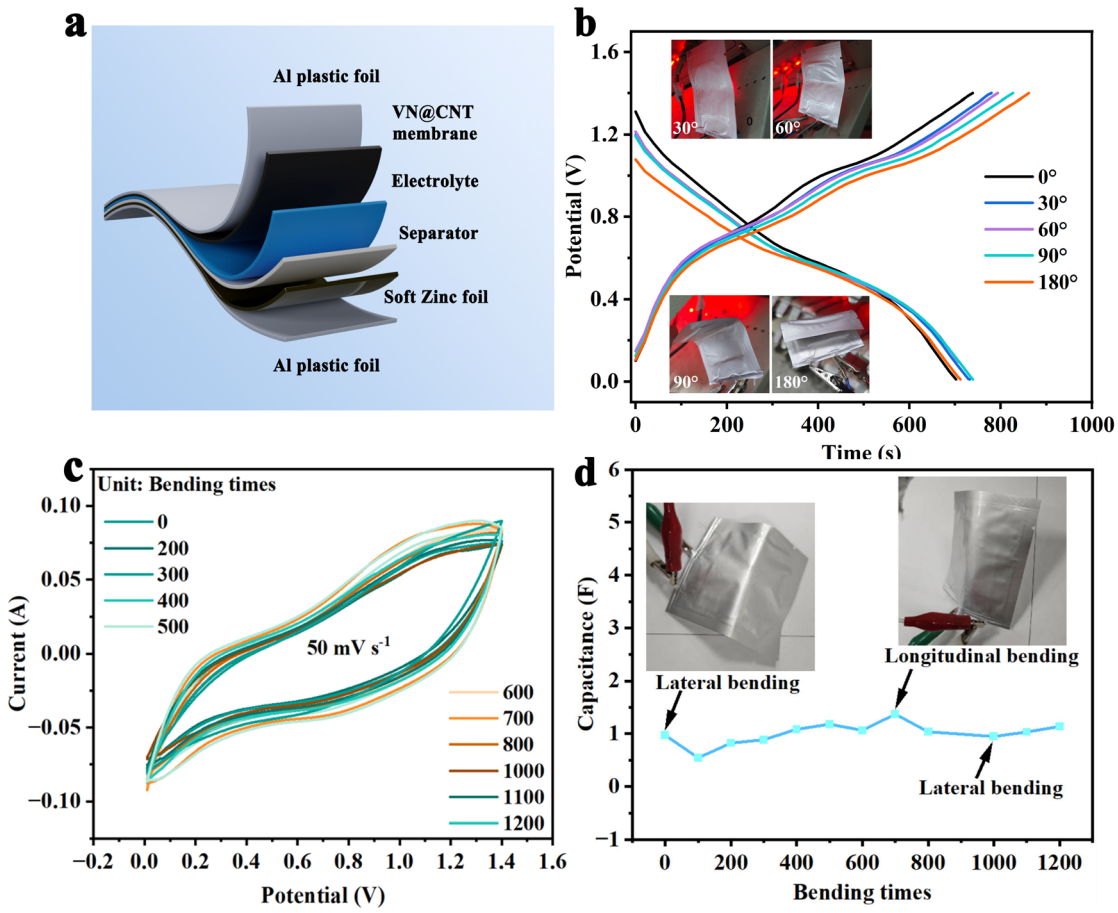

Fig. 5 Flexibility of the ZHSC device. (a) Schematic illustration of the flexible ZHSC device based on flexible VN@CNT membrane cathode materials. (b) GCD curves at a current density of 0.5 A g^{-1} of the flexible device in a flat state and at bending angles of 30°, 60°, 90°, and 180°, respectively. (c) The CV curves after different bending times, from 0–1200 times. (d) The capacitance delivered by the flexible ZHSC device was measured after undergoing a range of bending times, from 0–1200 times.

electrodes in flexible wearable electronics.[59] The retention of electrochemical performance after multiple bending cycles is crucial for the sustainable usability of flexible wearable devices, and thus the capacity retention rate post-bending has become a key indicator of the flexibility performance of such devices. We have conducted over a thousand bending tests on the device. Manual bending introduces more variability than mechanical bending and therefore more closely simulates real-life usage; this includes both lateral and longitudinal bending, with a specific bending process available in ESI 2.† As shown in Fig. 5c, there are no significant changes in the CV curves corresponding to 0–1200 bending times, indicating the device's tolerance to bending. Fig. 5d presents the specific capacitance corresponding to 0–1200 bending times, as calculated from the CV curves. After 100 bending cycles, there is a slight decrease in capacitance, which may be attributed to the device adjusting to the changes induced by bending. However, the specific capacitance fully recovers in the subsequent bends, and the fluctuations in capacitance after every 100 bends are minimal, suggesting that the material can fully withstand the number of bends encountered in daily use. Remarkably, after 1200 bends, the capacitance shows no degradation, demonstrating excellent mechanical flexibility and significant potential for practical applications.

4 Conclusions

In summary, this study has successfully fabricated a VN@CNT flexible electrode through a vacuum filtration and high-temperature nitridation strategy. s-XAS revealed that the 3d state of V e_g orbitals becomes occupied by electrons after the transition from V_2C@CNT to VN@CNT, leading to a reduction in valence states and an enhancement in metallicity. The electrical conductivity measured by the van der Pauw method shows an almost tenfold increase after nitridation, significantly improving the rate performance of the VN@CNT membrane as a cathode material for ZHSCs. At a high current density of 10 A g^{-1}, the device still maintains a high specific capacitance of 252.09 F g^{-1}, retaining 80.17% of its capacitance compared to that at 0.5 A g^{-1}. After 2000 charge–discharge cycles, it maintains 94.39% of its capacitance, demonstrating considerable cycling stability. The ZHSCs based on VN@CNT not only possess high power and energy densities but also exhibit excellent flexibility and bending resistance. The GCD curves and capacitance show no significant changes under multiple bending angles from 0 to 180°. Furthermore, even after 1200 repeated bending cycles, the capacity shows no degradation. The excellent electrochemical and flexible properties of the VN@CNT membrane electrodes prepared are verified in this study. Therefore, this research can not only guide the structural design of flexible electrode materials but also provide insights into the further development of flexible electronic devices.

Author contributions

Y. Y. Cao completed the experiment and writing. S. Q. Wei and S. M. Chen conceived the idea, directed the project, and mentored the manuscript writing and revision. Y. X. Wang and Q. Zhou participated in the experiments. Y. J. Xia, W. J. Xu, and C. D. Wang analyzed the data. L. Song supervised this project.

Conflicts of interest

There are no conflicts to declare.

Acknowledgements

This work was financially supported in part by the National Key R&D Program of China (2022YFA1605400), the National Natural Science Foundation of China (12322515, U23A20121 and 12225508), the Youth Innovation Promotion Association of CAS (2022457), the National Postdoctoral Program for Innovative Talents (BX20230346) and the China Postdoctoral Science Foundation (2023M743365). We thank the Shanghai Synchrotron Radiation Facility (BL14W1, BL14B1, and SSRF), the Beijing Synchrotron Radiation Facility (1W1B, 4B7A, and BSRF), the Hefei Synchrotron Radiation Facility (BL11U, BL10B, MCD-A and MCD-B Soochow Beamline for Energy Materials at NSRL), and the USTC Center for Micro and Nanoscale Research and Fabrication for help in characterization. This work was partially carried out at the Instruments Center for Physical Science, University of Science and Technology of China.

References

1 Y. Lin, Y. Gao and Z. Fan, *Adv. Mater.*, 2017, **29**, 1701736.
2 J. Lee, K. Cho and J. Kim, *Adv. Mater.*, 2024, **36**, 2310505.
3 J. Rao, N. Liu, Z. Zhang, J. Su, L. Li, L. Xiong and Y. Gao, *Nano Energy*, 2018, **51**, 425–433.
4 T. H. Han, H. Kim, S. J. Kwon and T. W. Lee, *Mater. Sci. Eng., R*, 2017, **118**, 1–43.
5 Y. Wang, W.-H. Zhong, T. Schiff, A. Eyler and B. Li, *Adv. Energy Mater.*, 2015, **5**, 1400463.
6 Z. Hong, Z. Fang, Y. Luo, H. Wu, H. Tian, F. Zhao, Q. Li, S. Fan and J. Wang, *J. Mater. Chem. A*, 2022, **10**, 23509–23520.
7 X. Cao, D. Tan, Q. Guo, T. Zhang, F. Hu, N. Sun, J. Huang, C. Fang, R. Ji, S. Bi and C. Jiang, *J. Mater. Chem. A*, 2022, **10**, 11562–11573.
8 C. Wang, S. Chen and L. Song, *Adv. Funct. Mater.*, 2020, **30**, 2000869.
9 N. Kamboj, B. B. Upreti, N. Kumar and R. S. Dey, *ACS Sustain. Chem. Eng.*, 2023, **11**, 5451–5461.
10 H. Zhang, Q. Liu, Y. Fang, C. Teng, X. Liu, P. Fang, Y. Tong and X. Lu, *Adv. Mater.*, 2019, **31**, 1904948.
11 Y. Lu, Z. Li, Z. Bai, H. Mi, C. Ji, H. Pang, C. Yu and J. Qiu, *Nano Energy*, 2019, **66**, 104132.
12 M. S. Javed, T. Najam, I. Hussain, M. Idrees, A. Ahmad, M. Imran, S. S. A. Shah, R. Luque and W. Han, *Adv. Energy Mater.*, 2023, **13**, 2202303.
13 P. Yu, Y. Zeng, H. Zhang, M. Yu, Y. Tong and X. Lu, *Small*, 2019, **15**, 1804760.
14 Y. Liu, Z. Sun, K. Tan, D. K. Denis, J. Sun, L. Liang, L. Hou and C. Yuan, *J. Mater. Chem. A*, 2019, **7**, 4353–4382.
15 N. Kamboj and R. S. Dey, *Electrochim. Acta*, 2022, **421**, 140499.

16 J. Pu, Q. Cao, Y. Gao, J. Yang, D. Cai, X. Chen, X. Tang, G. Fu, Z. Pan and C. Guan, *J. Mater. Chem. A*, 2021, **9**, 17292–17299.
17 C. Wang, Z. Pei, Q. Meng, C. Zhang, X. Sui, Z. Yuan, S. Wang and Y. Chen, *Angew. Chem., Int. Ed.*, 2021, **60**, 990–997.
18 M. S. Javed, H. Lei, Z. Wang, B. Liu, X. Cai and W. Mai, *Nano Energy*, 2020, **70**, 104573.
19 Y. Wang, G. Jiang, Z. Zhang, H. Chen, Y. Li, D. Kong, X. Qin, Y. Li, X. Zhang and H. Wang, *Energy Technol.*, 2022, **10**, 2101170.
20 Y. Lu, Y. Wen, F. Huang, T. Zhu, S. Sun, B. C. Benicewicz and K. Huang, *Energy Storage Mater.*, 2020, **27**, 418–425.
21 Y. G. Lee, J. Lee and G. H. An, *Chem. Eng. J.*, 2021, **414**, 128916.
22 P. Zhang, C. Wang, S. Wei, H. Shou, K. Zhu, Y. Cao, W. Xu, X. Guo, X. Wu, S. Chen and L. Song, *ACS Appl. Mater. Interfaces*, 2021, **13**, 61258–61266.
23 T. Ressler, *J. Synchrotron Radiat.*, 1998, **5**, 118–122.
24 S. Zhu, C. Wang, H. Shou, P. Zhang, P. Wan, X. Guo, Z. Yu, W. Wang, S. Chen, W. Chu and L. Song, *Adv. Mater.*, 2022, **34**, 2108809.
25 S. Wei, P. Zhang, W. Xu, S. Chen, Y. Xia, Y. Cao, K. Zhu, Q. Cui, W. Wen, C. Wu, C. Wang and L. Song, *J. Am. Chem. Soc.*, 2023, **145**, 10681–10690.
26 S. Wei, C. Wang, S. Chen, P. Zhang, K. Zhu, C. Wu, P. Song, W. Wen and L. Song, *Adv. Energy Mater.*, 2020, **10**, 1903712.
27 B. Asbani, K. Robert, P. Roussel, T. Brousse and C. Lethien, *Energy Storage Mater.*, 2021, **37**, 207–214.
28 Y. Wang, S. Wei, Z. H. Qi, S. Chen, K. Zhu, H. Ding, Y. Cao, Q. Zhou, C. Wang, P. Zhang, X. Guo, X. Yang, X. Wu and L. Song, *Proc. Natl. Acad. Sci. U.S.A.*, 2023, **120**, 2217208120.
29 W. L. Jang, Y. M. Lu, C. L. Chen, Y. R. Lu, C. L. Dong, P. H. Hsieh, W. S. Hwang, J. L. Chen, J. M. Chen, T. S. Chan, J. F. Lee and W. C. Chou, *Phys. Chem. Chem. Phys.*, 2014, **16**, 4699–4708.
30 D. Maganas, A. Trunschke, R. Schlogl and F. Neese, *Faraday Discuss.*, 2016, **188**, 181–197.
31 J. Li, K. McColl, X. Lu, S. Sathasivam, H. Dong, L. Kang, Z. Li, S. Zhao, A. G. Kafizas, R. Wang, D. J. L. Brett, P. R. Shearing, F. Corà, G. He, C. J. Carmalt and I. P. Parkin, *Adv. Energy Mater.*, 2020, **10**, 2000058.
32 L. R. De Jesus, Y. Zhao, G. A. Horrocks, J. L. Andrews, P. Stein, B.-X. Xu and S. Banerjee, *J. Mater. Chem. A*, 2017, **5**, 20141–20152.
33 K. Zhu, Q. Zhu, M. Jiang, Y. Zhang, Z. Shao, Z. Geng, X. Wang, H. Zeng, X. Wu, W. Zhang, K. Huang and S. Feng, *Angew. Chem., Int. Ed.*, 2022, **61**, 202207600.
34 C. Wang, S. Chen, H. Xie, S. Wei, C. Wu and L. Song, *Adv. Energy Mater.*, 2018, **9**, 1802977.
35 J. H. Guo, Report Number: LBNL-58896, United States, 2005.
36 G. A. Rooke, *J. Res. Natl. Bur. Stand.*, 1970, **74**, 273–279.
37 L. Zhang, G. Wang, J. Feng, Q. Ma, Z. Liu and X. Yan, *ChemElectroChem*, 2021, **8**, 1289–1297.
38 S. Xu, X. Tan, W. Ding, W. Ren, Q. Zhao, W. Huang, J. Liu, R. Qi, Y. Zhang, J. Yang, C. Zuo, H. Ji, H. Ren, B. Cao, H. Xue, Z. Gao, H. Yi, W. Zhao, Y. Xiao, Q. Zhao, M. Zhang and F. Pan, *Angew. Chem.*, 2023, **135**, e202218595.
39 R. Tian, N. Alcala, S. J. K. O'Neill, D. V. Horvath, J. Coelho, A. J. Griffin, Y. Zhang, V. Nicolosi, C. O'Dwyer and J. N. Coleman, *ACS Appl. Energy Mater.*, 2020, **3**, 2966–2974.
40 J. L. Andrews, A. Mukherjee, H. D. Yoo, A. Parija, P. M. Marley, S. Fakra, D. Prendergast, J. Cabana, R. F. Klie and S. Banerjee, *Chem*, 2018, **4**, 564–585.
41 W. Jang, Y. Lu, C. Chen, Y. Lu, C. Dong, P. Hsieh, W. Hwang, J. Chen, J. Chen, T. Chan, J. Lee and W. Chou, *Phys. Chem. Chem. Phys.*, 2014, **16**, 4699–4708.
42 N. Zhang, L. Cao, L. Feng, J. Huang, K. Kajiyoshi, C. Li, Q. Liu, D. Yang and J. He, *Nanoscale*, 2019, **11**, 11542–11549.
43 Y. Wu, L. Fan, Q. Liu, S. Chen, W. Huang, F. Chen, G. Liao, C. Zou and Z. Wu, *Sci. Rep.*, 2015, **5**, 9328.
44 Q. Yang, Z. Huang, X. Li, Z. Liu, H. Li, G. Liang, D. Wang, Q. Huang, S. Zhang, S. Chen and C. Zhi, *ACS Nano*, 2019, **13**, 8275–8283.
45 P. Lian, Y. Dong, Z. Wu, S. Zheng, X. Wang, W. Sen, C. Sun, J. Qin, X. Shi and X. Bao, *Nano Energy*, 2017, **40**, 1–8.
46 C. E. Ren, M. Zhao, T. Makaryan, J. Halim, M. Boota, S. Kota, B. Anasori, M. W. Barsoum and Y. Gogotsi, *ChemElectroChem*, 2016, **3**, 689–693.
47 Y. Cao, S. Wei, Q. Zhou, P. Zhang, C. Wang, K. Zhu, W. Xu, X. Guo, X. Yang, Y. Wang, X. Wu, S. Chen and L. Song, *2D Mater.*, 2023, **10**, 014001.
48 S. Liu, L. Kang, J. M. Kim, Y. T. Chun, J. Zhang and S. C. Jun, *Adv. Energy Mater.*, 2020, **10**, 2000477.
49 Y. Jiang, K. Ma, M. Sun, Y. Li and J. Liu, *Energy Environ. Mater.*, 2023, **6**, e12357.
50 F. Liang, M. Chen, S. Zhang, Z. Zou, C. Ge, S. Jia, S. Le, F. Yu and J. Nong, *ACS Sustain. Chem. Eng.*, 2024, **12**, 5117–5128.
51 S. Y. Luchkin, M. A. Kirsanova, D. A. Aksyonov, S. A. Lipovskikh, V. A. Nikitina, A. M. Abakumov and K. J. Stevenson, *ACS Appl. Energy Mater.*, 2022, **5**, 7758–7769.
52 Y. Guo, C. Luo, M. Yang, H. Wang, W. Ma, K. Hu, L. Li, F. Wu and R. Chen, *Angew. Chem., Int. Ed.*, 2024, e202406597.
53 Q. Wang, S. Wang, X. Guo, L. Ruan, N. Wei, Y. Ma, J. Li, M. Wang, W. Li and W. Zeng, *Adv. Electron. Mater.*, 2019, **5**, 1900537.
54 Y. Zhu, X. Ye, H. Jiang, J. Xia, Z. Yue, L. Wang, Z. Wan, C. Jia and X. Yao, *J. Power Sources*, 2020, **453**, 227851.
55 M. Peng, L. Wang, L. Li, X. Tang, B. Huang, T. Hu, K. Yuan and Y. Chen, *Adv. Funct. Mater.*, 2021, **32**, 2109524.
56 C. Wang, H. Xie, S. Chen, B. Ge, D. Liu, C. Wu, W. Xu, W. Chu, G. Babu, P. M. Ajayan and L. Song, *Adv. Mater.*, 2018, **30**, 1802525.
57 H. Jiang, Y. Zhang, Y. Liu, J. Yang, L. Xu, P. Wang, Z. Gao, J. Zheng, C. Meng and Z. Pan, *J. Mater. Chem. A*, 2020, **8**, 15130–15139.
58 X. Li, Y. Tang, H. Lv, W. Wang, F. Mo, G. Liang, C. Zhi and H. Li, *Nanoscale*, 2019, **11**, 17992–18008.
59 C. Wang, C. Wu, S. Chen, X. Zhao, W. Xu, Z. Niu and L. Song, *Carbon*, 2017, **125**, 419–428.